Anisotropic optical properties of silver nanoparticle arrays on rippled dielectric surfaces produced by low-energy ion erosion

S. Camelio,* D. Babonneau, D. Lantiat,† L. Simonot, and F. Pailloux
Laboratoire de Physique des Matériaux (PHYMAT), UMR 6630 CNRS, Université de Poitiers, SP2MI, Téléport 2, Boulevard Marie et Pierre Curie, BP 30179, 86962 Futuroscope Chasseneuil Cedex, France
(Received 9 March 2009; revised manuscript received 8 September 2009; published 15 October 2009)

Nanoripple patterns with long-range order have been fabricated on amorphous dielectric films by Xe^+ ion etching. They are used as templates to elaborate organized arrays of aligned Ag nanoparticles by grazing incidence ion-beam sputtering. The particles present an ellipsoidal shape with a major axis parallel to the ripples. Optical calculations show that both the spatial organization and shape anisotropies contribute to a strong dependence of the surface-plasmon resonance of the nanocomposite films on the orientation of the electric field.

DOI: 10.1103/PhysRevB.80.155434 PACS number(s): 61.46.−w, 78.67.−n, 81.07.−b

I. INTRODUCTION

Metal nanoparticles show peculiar properties different from those of bulk materials that make them attractive for many applications ranging from nanophotonics[1–3] to biochemistry.[4,5] Indeed, the optical response of noble-metal nanoparticles is dominated by the surface-plasmon resonance (SPR) phenomenon, which induces both a wavelength-selective photon absorption in the visible range and a strong enhancement of the local electromagnetic field inside and near the particles that make them interesting for surface-enhanced Raman-scattering measurements and its applications for molecular detection.[6] The spectral position of the SPR not only depends on the intrinsic properties of the metal and of the dielectric matrix surrounding the particles, on the chemical nature of the metal/dielectric interface, but is also affected by the morphology (shape and size) and spatial organization of the metallic particles within the matrix.[7,8]

In previous works,[9–12] we have investigated in detail the morphology of Ag nanoparticles capped by various dielectric matrices (BN, Si_3N_4, Al_2O_3, and Y_2O_3). We have shown that when the growth is performed on atomically flat substrates, the nanoparticles are randomly distributed on the surface and present an out-of-plane aspect ratio (H/D) strongly dependent on the matrix. Moreover, a quantitative structural analysis by high-angle annular dark-field scanning transmission electron microscopy (HAADF-STEM) has revealed a linear increase in the height of the individual nanoparticles with their in-plane diameter, independently of the deposited metal amount.[11,12] This behavior is believed to originate from a delicate interplay between thermodynamics and kinetics. Therefore, by adjusting the nature of the matrix, it is possible to change the optical properties of the nanocomposite films by the modification of the dielectric environment of the nanoparticles and the induced change in nanoparticle shape.

A new route to control not only the morphology but also the in-plane organization of the nanoparticles, and therefore their physical properties, is to use nanostructured surfaces as templates.[13–22] In a recent study,[21] we have shown that faceted alumina substrates prepared by thermal treatment of vicinal surfaces can be used to obtain organized arrays of nanoparticles by self-shadowing effects under grazing incidence during the metal deposition. According to the orientation of the atomic beam compared to the facets and the incidence angle, it is possible to select the type of facet on which the growth takes place and consequently to elaborate organized systems constituted of stripes or linear chains of particles. The structural anisotropy of these systems results in a dependence of their optical response on the orientation of the electric field. However, while promising, the preparation technique requires extreme temperature (>1000 °C) for the template production and the choice of substrate is limited to crystalline materials. To take advantage of tuning the spectral position of the SPR by the control of the optical properties of the matrix, it is necessary to widen the type of nanostructured templates on which the nanoparticles are deposited. Moreover, the synthesis of organized arrays in a "one-step process" over a large scale in time-saving conditions at mild temperature is very attractive for nanotechnology applications. It is known that surface etching by ion sputtering at oblique incidence of amorphous bulk materials such as SiO_2,[22–24] as well as crystalline semiconductors[18,19,25–27] or metals[28] can produce regular repetitive and periodic surface structures in the form of ripples. The phenomenon is related to the interplay between ion erosion and the diffusion of adatoms, which induces surface reorganization. This technique can be applied to a large variety of fabrication process allowing the *in situ* production of surfaces with well-defined lateral periodicity, vertical amplitude, and controlled orientation.[29,30] This paper reports on the broader applicability of such method to amorphous dielectric thin films (BN, Si_3N_4, and Al_2O_3) and on the realization of metallic nanoparticle arrays. Depending on the nature of the material, the energy of the incident ion beam and the etching duration, we show that nanopatterning of the dielectric films with different periods and amplitudes is possible. Furthermore, metallic nanoparticle arrays can be obtained by silver sputtering at grazing incidence on such templates. Finally, we demonstrate that the Al_2O_3-capped silver nanoparticles exhibit anisotropic optical properties which are interpreted as the consequence of two contributions: in-plane organization and shape anisotropy.

II. EXPERIMENT

All the experiments were performed at room temperature in a Dual Ion Beam Sputtering Nordiko™ chamber (base

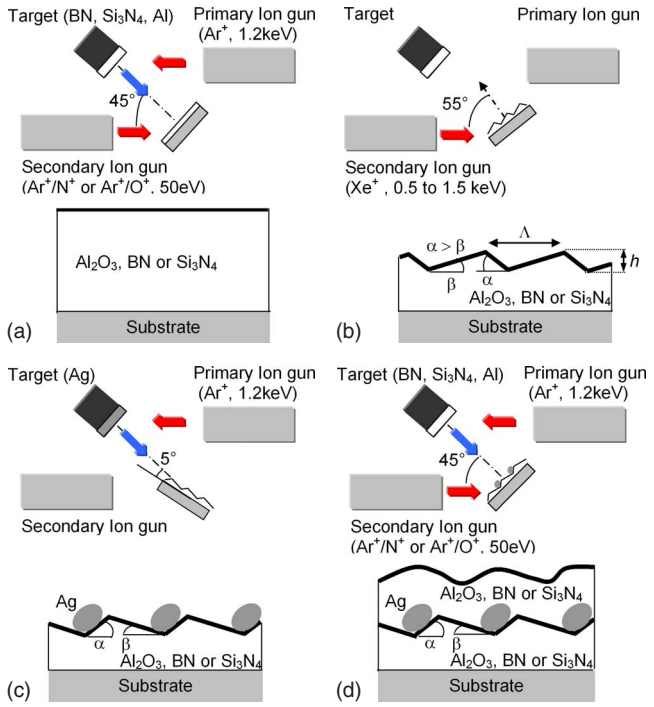

FIG. 1. (Color online) Schematic of the nanostructure elaboration process: (a) amorphous dielectric buffer-layer deposition at normal incidence, (b) etching of the buffer layer with Xe^+ ions at 55° with respect to the surface normal, (c) deposition of silver at grazing incidence (5° with respect to the surface), and (d) deposition of the amorphous dielectric capping layer at normal incidence.

pressure 4×10^{-8} Torr) consisting of two rf-plasma ion guns. The elaboration process started with the deposition at normal incidence of an amorphous dielectric buffer layer by sputtering of a BN, Si_3N_4, or Al target with a primary Ar^+ ion gun operated at 1.2 kV with a current of 80 mA. To obtain the correct stoichiometry, the deposition of the buffer layer was assisted by a secondary-ion beam (Ar^+/N^+ or Ar^+/O^+ with an energy of 50 eV and a current of 40 mA) oriented at 45° with respect to the surface normal [Fig. 1(a)]. The secondary-ion gun was then used to etch the surface of the dielectric buffer layer at 55° with respect to the normal in order to develop ripples with long-range order [Fig. 1(b)]. The intensity of the secondary-ion gun was fixed at 40 mA (flux in the range of 2×10^{14} ions cm^{-2} s^{-1}) while the voltage applied to the grids was varied from 0.5 to 1.5 kV. The thicknesses of the buffer layers were measured before and after Xe^+ etching by spectroscopic ellipsometry. As reported in Table I, the etching rates were in the range from 0.2 to 0.7 nm/s depending on the material and ion energy.

The elaboration of nanoparticle arrays on nanopatterned dielectric surfaces is sketched in Figs. 1(c) and 1(d): an effective Ag thickness of 2 nm was deposited at a grazing incidence of 5° with respect to the surface on a 80-nm-thick Al_2O_3 thin film etched by 1 keV-Xe^+ ions during 180 s, with a Ag beam direction antiparallel to the direction of the Xe^+ beam [Fig. 1(c)]. Furthermore, after a delay time of 30 min, which enables the nanoparticle shape to reach an equilibrium state,[10] an additional 20-nm-thick amorphous Al_2O_3 capping layer was deposited at normal incidence to preserve silver from the external environment [Fig. 1(d)].

Structural characterization of the nanostructured surfaces and of the buried nanoparticles was performed by *ex situ* atomic force microscopy (AFM) in the tapping mode, by HAADF-STEM with a JEOL 2200FS microscope using an acceleration voltage of 200 kV, a probe size of 0.7 nm and an inner collection angle of 50 mrad, and by grazing incidence small-angle x-ray scattering (GISAXS). The GISAXS data were collected at the European Synchrotron Radiation Facility (Grenoble, France) with the small-angle scattering setup of the D2AM beamline. The energy of the incident x-ray beam was fixed at 11.7 keV and the angle of incidence, $\alpha_i=0.20°$, was close to the critical angle for total external reflection of Al_2O_3. The optical response of the nanoparticles was investigated by transmittance measurements under normal incidence between 350 and 800 nm with a 5 nm monochromator step. Substrates were commercially available epipolished Si(001) wafers covered with a native SiO_2 layer for ellipsometry and x-ray measurements, fused silica for optical measurements, and freshly cleaved NaCl for TEM characterizations. The films deposited on NaCl were floated in purified water and the resulting freestanding thin films were collected on microscope grids.

TABLE I. Parameters retrieved from ellipsometric and GISAXS measurements of dielectric thin films etched with Xe^+ ions at 55° with respect to the surface normal: buffer thickness before etching, etched thickness, ripple period Λ and standard deviation σ_Λ, ripple amplitude h, positive slope β, and negative slope α resulting from the profile asymmetry of the ripples [see Fig. 1(b)] for different dielectric materials, different Xe^+ energies, and different etching durations.

Dielectric material	Xe^+ energy (keV)	Etching duration (s)	Buffer thickness (nm)	Etched thickness (nm)	Etching rate (nm/s)	Λ (nm)	σ_Λ (nm)	h (nm)	α (°)	β (°)
Al_2O_3	1.0	90	45	32	0.35	20.6	5.1	0.8	6.1	3.7
Al_2O_3	1.0	180	80	67	0.37	21.4	4.3	3.8	22.3	17.6
Al_2O_3	1.0	360	170	123	0.34	22.8	4.2	3.9	26.6	21.5
Al_2O_3	0.5	120	45	25.5	0.21	14.4	3.0	2.7	20.9	20.0
Al_2O_3	1.3	100	113	46	0.46	22.4	4.6	3.8	20.4	17.6
Al_2O_3	1.5	90	113	46	0.51	24.3	5.4	3.6	16.7	16.0
BN	1.0	100	83	31	0.31	14.4	3.2	4.1	39.9	23.2
Si_3N_4	1.0	100	85	67	0.67	18.6	4.9	3.0	20.1	16.0

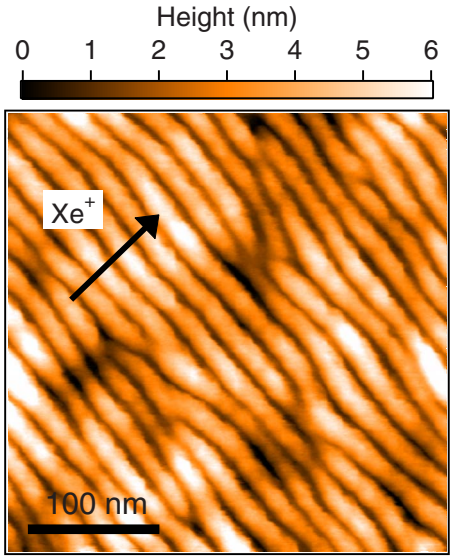

FIG. 2. (Color online) AFM topographic image of a 170-nm-thick Al_2O_3 thin film etched during 180 s with 1 keV-Xe^+ ions at 55° with respect to the surface normal, i.e., after the removal of 67 nm of material. The projection of the Xe^+ beam direction onto the surface is indicated by the arrow.

III. RESULTS AND DISCUSSION

A. Nanoripple patterns on dielectric surfaces

As a typical example, Fig. 2 displays the surface topography obtained by AFM of a 170-nm-thick Al_2O_3 thin film etched during 180 s with 1 keV-Xe^+ ions, i.e., after 67 nm of the material is sputtered. According to Ref. 29, the ripples are perpendicular to the ion-beam projection, with a period $\Lambda = 23 \pm 1$ nm (obtained from the autocorrelation function of the image) and a mean amplitude $h = 2.2 \pm 0.8$ nm. Let us note that this amplitude may be underestimated because of tip artifact since the radius of curvature of the tip, around 10 nm, is not negligible compared to the ripple period. GISAXS experiments can also give statistical information on the surface topography with a probed area of about 0.5 mm × 15 mm. Figure 3(a) shows the two-dimensional (2D) GISAXS pattern of a 80-nm-thick Al_2O_3 thin film etched by 1 keV-Xe^+ ions during 180 s, with the incident x-ray beam oriented parallel to the ripples. The formation of ripples with long-range order is revealed by the presence of two intense and sharp streaks located at $q_y = \pm 0.24$ nm^{-1} on both sides of the vertical beam stop. The ripple period is inversely proportional to the separation of the streaks in the q_y direction and the amplitude of the ripples is inversely proportional to the extend of the streak intensity in the q_z direction. In addition, it is worth noting that the intensity of the streak on the positive q_y side is slightly higher than the one on the negative q_y side. This diffuse intensity asymmetry was also observed by Umbach *et al.*[24] and Zhou *et al.*[31] in the case of Ar^+-eroded SiO_2 and sapphire substrates, respectively, and ascribed to an asymmetric profile of the rippled surface. The quantitative analysis of the 2D GISAXS pattern was performed in the framework of the distorted wave-Born approximation[32] with a homemade package[33] developed

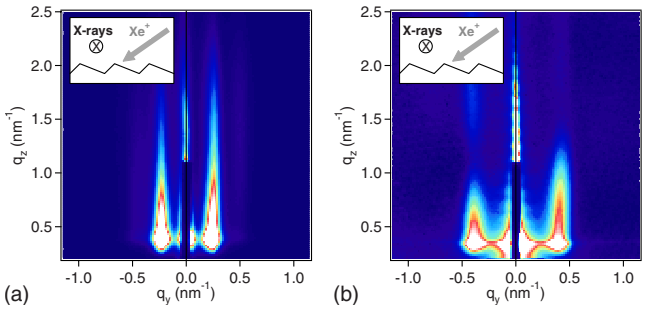

FIG. 3. (Color online) (a) 2D GISAXS pattern of a 80-nm-thick Al_2O_3 thin film etched during 180 s with 1 keV-Xe^+ ions at 55° with respect to the surface normal. (b) 2D GISAXS pattern of a 83-nm-thick BN thin film etched with 1 keV-Xe^+ ions during 100 s at 55° with respect to the surface normal. The direction of the x-ray beam is parallel to the ripples and the direction of the Xe^+ flux is indicated by arrows.

within the IGOR PRO Analysis software (WaveMetrics, Inc.). An asymmetric sawtooth profile with a positive slope β and a negative slope α [sketched in Fig. 1(b)] was used as a simplified approximation to the ripple shape. The interference function (i.e., the Fourier transform of the ripple position autocorrelation function) was calculated in the framework of the paracrystal model[34] assuming a Gaussian probability of the ripple spacing specified by an average spacing Λ and a standard deviation σ_Λ. In the case of the 80-nm-thick Al_2O_3 thin film etched by 1 keV-Xe^+ ions during 180 s [Fig. 3(a)], the best-fit parameters given in Table I are $\Lambda = 21.4$ nm, $\sigma_\Lambda = 4.3$ nm, $\alpha = 22.3°$, and $\beta = 17.6°$, thus yielding a mean ripple amplitude $h = \Lambda \frac{\tan\alpha \tan\beta}{\tan\alpha + \tan\beta} = 3.8$ nm. The period Λ and amplitude h retrieved from GISAXS measurements are therefore consistent with the ones obtained with AFM. Aspect ratios $\frac{h}{\Lambda}$ of 0.18 or less (see Table I) are observed from GISAXS measurements, which also show a strong sensitivity to the slight asymmetry of the ripples profile. AFM images can provide information on the ripple asymmetry but since the probed area in GISAXS measurements is less local than the one probed with AFM, slopes and ripples amplitudes retrieved from the quantitative GISAXS analysis are relevant to the mean topography of the sample.

It has been shown that the period and the amplitude of the ripples depend on the nature of the etched material and can be varied by adjusting the nature and energy of the ions, the etching duration, the surface temperature, and the incidence angle.[27,29–31] To illustrate this point, we show in Fig. 3(b) the 2D GISAXS pattern of a 83-nm-thick BN thin film etched with 1 keV-Xe^+ ions during 100 s at 55° with respect to the surface normal. In comparison with the 80-nm-thick Al_2O_3 thin film etched at the same energy [Fig. 3(a)], a visual inspection of the 2D GISAXS patterns reveals that the period of the ripples is smaller for the BN film and the asymmetry is more pronounced. We also present in Table I the morphological parameters of the ripples obtained from GISAXS measurements as a function of the ion energy, the etching duration and the dielectric material. For 1 keV-Xe^+ ions, the increase in the etching duration of the Al_2O_3 thin films from 90 to 180 s causes a rapid increase in the ripple amplitude h associated to a decrease in the period standard deviation σ_Λ

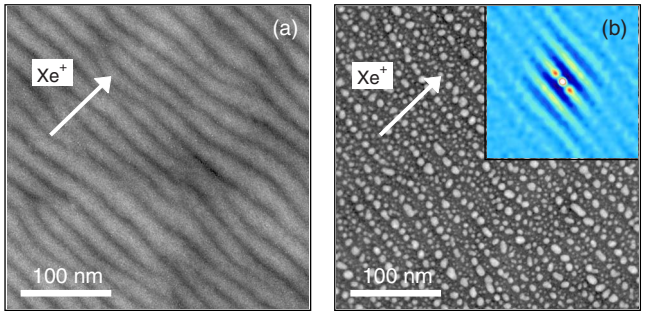

FIG. 4. (Color online) Plane-view HAADF-STEM images of a 80-nm-thick Al_2O_3 thin film etched during 180 s with 1 keV-Xe^+ ions at 55° with respect to the surface normal (a) before and (b) after deposition at grazing incidence of Al_2O_3-capped Ag nanoparticles. The projection of the Xe^+ beam direction onto the surface is indicated by the arrow. Inset: corresponding autocorrelation function (same scale as the HAADF-STEM image).

(which means that the ordering of the ripples is improved) but the period Λ remains relatively constant. For longer sputtering time (360 s), the growth of the pattern tends to saturate. The reduction in the Xe^+ energy from 1.5 to 0.5 keV allows one to reduce the period of the ripples from 24.3 to 14.4 nm. This behavior is consistent with results reported in the literature showing that the ripple period often scales with energy.[30] Furthermore, the results confirm that the period of the ripples is smaller and the asymmetry is higher for BN than the ones obtained with Al_2O_3 for a same quantity of removed material. As concerned the Si_3N_4 buffer, the etching rate is higher than the one obtained with BN and Al_2O_3 and the ripples present a period and an amplitude slightly lower than the ones found for Al_2O_3. During the sputtering, the surface is far from equilibrium and the formation of the ripple structure is the expression of a dynamic balance among surface kinetic processes such as erosion, ion-induced defect creation, and diffusion. Some of these surface processes induce roughening (e.g., sputtering of atoms off the surface) and others induce smoothing (e.g., diffusion of defects).[29,30] Therefore the dynamic competition among these different processes strongly depends on the material under sputtering and it is not surprising that the different thin films presented in this study show different topographies (period, amplitude, and profile asymmetry). From these different results, it appears that it is possible to achieve a tailor-made nanopatterning of amorphous dielectric matrices with periods and amplitudes ranging from 15 to 25 nm and from 1 to 4 nm, respectively. Moreover, the ripple period is also known to depend on temperature[29,30] and we can anticipate an increase in the period when performing etching at higher temperatures.

B. Nanoparticle linear array

1. Structural analysis

Figure 4(a) displays the morphology of a rippled Al_2O_3 buffer layer (etched with 1 keV-Xe^+ ions) before silver deposition as imaged by HAADF-STEM. By collecting high-angle scattered electrons, almost only incoherent Rutherford scattering contributes to the image[35] and thereby, the collected intensity is approximately proportional to the square of the atomic number Z (Z-contrast imaging) and to the atomic column occupancy, i.e., the thickness of the film. The contrast of intensity obtained in the image presented in Fig. 4(a) is thus due to the presence of the ripples. After deposition of the $Ag:Al_2O_3$ nanocomposite film (with a silver effective thickness of 2 nm) on such a one-dimensional rippled surface [Fig. 4(b)], the shadowing effect allows producing highly aligned Ag nanoparticles along the ripples, as recently obtained in the case of facetted NaCl and Al_2O_3 surfaces[13,20,21] or with Ar^+ ion-etched Si and glass substrates.[18,19,22] It should be pointed out in Fig. 4(b) that the size distribution is bimodal with small particles (diameter <4 nm) intercalated among lines of larger particles. Nevertheless, the surface coverage of the small particles is weak (2%) compared to the surface coverage of the large ones (20%) and consequently, their equivalent volume is negligible compared to the equivalent volume of the larger particles. These latter present an elongated shape in the direction parallel to the ripples. The mean center-to-center distance between the particles along the directions parallel $\langle L_{\parallel}\rangle$ and perpendicular $\langle L_{\perp}\rangle$ to the ripples have been found from the quantitative analysis of the autocorrelation function of the image given in the inset of Fig. 4(b). The areal density d and the size of the individual particles were retrieved from the analysis of the HAADF-STEM plane-view image by using the quantitative method described in a previous paper.[11] The nanoparticles were assumed to be semiellipsoidal with in-plane mean axes $\langle D_{\parallel}\rangle$ and $\langle D_{\perp}\rangle$ and a mean height $\langle H\rangle$. All the values are given in Table II. As obtained in previous studies,[9–12] the particles are flattened and present an D-dependent in-plane aspect ratio H/D (not shown). Finally, let us note that the nanoparticles show not only an anisotropic in-plane organization (with $\langle L_{\parallel}\rangle/\langle L_{\perp}\rangle=0.64$) but also an anisotropic shape (with $\langle D_{\parallel}\rangle/\langle D_{\perp}\rangle=1.23$).

Figure 5(a) displays the GISAXS pattern of the nanocomposite film obtained with the x-ray beam parallel to the

TABLE II. Particle density d, mean interparticle distance along the ripples $\langle L_{\parallel}\rangle$ and perpendicular to the ripples $\langle L_{\perp}\rangle$, mean height of the particles $\langle H\rangle$ and standard deviation σ_H, mean axis along the ripples $\langle D_{\parallel}\rangle$ and perpendicular to the ripples $\langle D_{\perp}\rangle$ and associated standard deviations $\sigma_{D_{\parallel}}$ and $\sigma_{D_{\perp}}$, and weighted height $\hat{H}$, diameter along the ripples $\hat{D}_{\parallel}$ and perpendicular to the ripples $\hat{D}_{\perp}$ used to simulate the optical transmittance spectra.

d (μm^{-2})	$\langle L_{\parallel}\rangle$ (nm)	$\langle L_{\perp}\rangle$ (nm)	$\langle H\rangle$ (nm)	σ_H (nm)	$\langle D_{\parallel}\rangle$ (nm)	$\sigma_{D_{\parallel}}$ (nm)	$\langle D_{\perp}\rangle$ (nm)	$\sigma_{D_{\perp}}$ (nm)	$\hat{H}$ (nm)	$\hat{D}_{\parallel}$ (nm)	$\hat{D}_{\perp}$ (nm)
4800	12.0	18.8	5.0	0.8	7.8	2.2	6.9	2.0	5.3	9.5	7.7

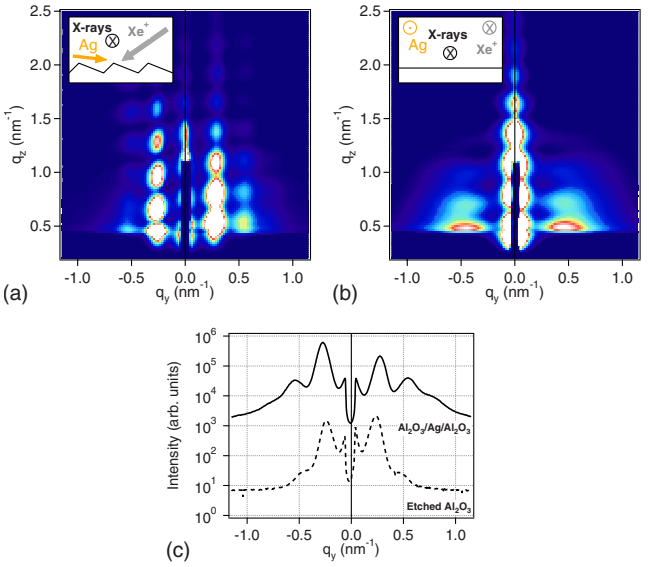

FIG. 5. (Color online) 2D GISAXS patterns of the Al_2O_3-capped Ag nanoparticles deposited at grazing incidence on a 80-nm-thick Al_2O_3 buffer layer etched during 180 s with 1 keV-Xe^+ ions with the direction of the x-ray beam (a) parallel and (b) perpendicular to the ripples. The directions of the Xe^+ and Ag flux are indicated by arrows. (c) Horizontal cross sections drawn at q_z=0.45 nm^{-1} before (dashed line) and after (solid line) Ag deposition and Al_2O_3 capping.

ripples. As for the case of the Al_2O_3 buffer layer [Fig. 3(a)], two intense and sharp streaks are exhibited on both sides of the vertical beam stop at $q_y = \pm 0.27$ nm^{-1}. These results show that the Ag nanoparticles replicate the long-range order between ripples in the lateral direction,[15] otherwise the GISAXS signal from Ag nanoparticles would be located at a different q_y position. In contrast, the 2D GISAXS pattern obtained with the x-ray beam perpendicular to the ripples [Fig. 5(b)] shows two broad lobes located at $q_y = \pm 0.47$ nm^{-1} typical of a 2D distribution of nanoparticles with only short-range order in a direction parallel to the ripples. Moreover, modulations of intensity are generated in the q_z direction in both Figs. 5(a) and 5(b) with a well-defined period, Δq_z, inversely proportional to the thickness of the Al_2O_3 capping layer, $t_{Al_2O_3}$ ($\Delta q_z = 2\pi / t_{Al_2O_3}$). These modulations are coming from correlated roughness effects, meaning that the topography of the Ag nanoparticles is partially replicated to the surface of the Al_2O_3 capping layer in the vertical direction[36,37] [Fig. 1(d)]. Furthermore, as shown in Fig. 5(c) the asymmetry of the GISAXS signal is reversed after Ag deposition (i.e., the intensity of the streak on the positive q_y side becomes smaller than the one on the negative q_y side), thus indicating that the Ag nanoparticles nucleates preferentially on the facets of the rippled surface that are illuminated during the Ag deposition [Fig. 1(c)].[13,22] These results suggest also that the small particles seen in HAADF-STEM image [Fig. 4(b)], which contribute weakly to the GISAXS signal, are located on the shadowed facets.

2. *Optical properties: Results and discussion*

The optical properties of the $Al_2O_3/Ag/Al_2O_3$ nanocomposite film deposited on a SiO_2 substrate have been studied

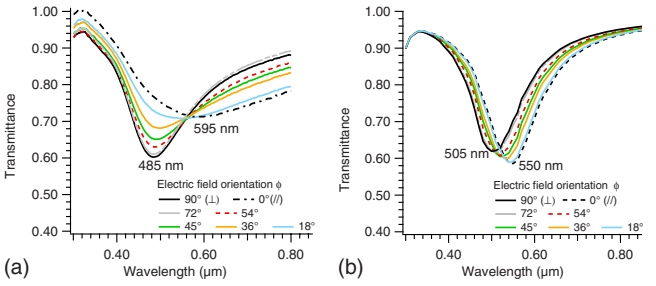

FIG. 6. (Color online) (a) Transmission measurements at normal incidence of the Al_2O_3-capped Ag nanoparticles deposited at grazing incidence on a 80-nm-thick Al_2O_3 buffer layer etched during 180 s with 1 keV-Xe^+ ions, with different orientations ϕ of the electric field with respect to the ripples direction. (b) Transmission calculations assuming a rectangular array of spheroidal Ag nanoparticles whose parameters ($\langle L_{\parallel} \rangle$, $\langle L_{\perp} \rangle$, and $\hat{H}$) are given in Table II and $\hat{D}$=8.2 nm. Different orientations ϕ of the electric field with respect to the ripples direction are considered.

by transmission measurements at normal incidence, with different orientations ϕ of the electric field with respect to the ripples direction. The experimental curves presented in Fig. 6(a) are normalized to the transmission of the Al_2O_3 buffer layer deposited on a SiO_2 substrate. A large splitting of the curves is clearly visible: for an in-plane orientation of the electric field ϕ=90° (i.e., perpendicular to the particles lines) down to ϕ=36°, the sample exhibits a SPR located at $\lambda_{\perp}$=485 nm while the SPR band is broadened and red-shifted to $\lambda_{\parallel}$=595 nm for an electric field parallel to the ripples (ϕ=0°). In addition, the shape of the SPR becomes asymmetric when ϕ decreases and is clearly a mix of both contributions when the field is oriented at ϕ=18°. Such red-shift and splitting of the SPR when the electric field is perpendicular or parallel to particles lines have already been observed[17,18,20,21] and are commonly attributed especially to the anisotropic spatial organization of the nanoparticles with a preferential electromagnetic coupling of the nanoparticles between the lines. Therefore, the optical transmittance spectra have been simulated by using the quantitative topographic and morphologic data retrieved from the HAADF-STEM analysis as input parameters. The calculations have been done by considering a three-layer structure ($Al_2O_3/Ag:Al_2O_3/Al_2O_3$) on a SiO_2 substrate. The dielectric functions of the substrate and of the Al_2O_3 films have been obtained from the bulk SiO_2 dielectric function and from spectroscopic ellipsometry measurements, respectively. A model based on the Yamaguchi theory[38] (see Appendix) has been used to determine the dielectric function of the $Ag:Al_2O_3$ nanocomposite layer: the particles are considered as identical electrostatic dipoles regularly located on a rectangular array (with lattice parameters $\langle L_{\parallel} \rangle$ and $\langle L_{\perp} \rangle$) and the particle shape as well as the interactions between particles are taken into account (no mirror image in this case since the nature of the buffer and capping layers surrounding the particles are the same).

The effective dielectric function ϵ_{eff} of the nanocomposite layer is given by

$$\epsilon_{\text{eff}} = \epsilon_{\text{cap}}\left[q\frac{\epsilon_{\text{m}} - \epsilon_{\text{cap}}}{\epsilon_{\text{cap}} + F(\epsilon_{\text{m}} - \epsilon_{\text{cap}})} + 1 \right], \quad (1)$$

where ϵ_{cap} is the dielectric function of the Al_2O_3 capping film, ϵ_{m} is the dielectric function of the metal determined from the bulk Ag dielectric function with a correction term,[7,39] which includes both size and interface effects: the corrected frequency collision is $\Gamma = \Gamma_0 + A\frac{v_f}{R}$, with $\Gamma_0 = \frac{v_f}{l}$ the frequency collision in bulk metal, v_f the Fermi velocity, l the mean-free path in bulk metal, R the radius of the particles, and A a fitting parameter (called in this paper damping factor), which reflects the intensity of the size effects and depends on the nature of the particle/matrix interface. q is the volume filling factor of the metallic nanoparticles inside the film, and F is an effective depolarization factor, which takes into account the shape of particles, the interparticle dipolar interactions, and the nature of the substrate.

The optical dichroism is often attributed to the in-plane organization of the nanoparticles.[17,20] Moreover, the optical response being dominated by the larger particles, the simulations were first performed assuming a set of regularly distributed nanoparticles with an identical spheroidal shape (i.e., by neglecting the in-plane shape anisotropy) with in-plane diameter $\hat{D}$ and height $\hat{H}$ given by

$$\hat{x} = \sum_{n=1}^{N} x_n V_n / \sum_{n=1}^{N} V_n \quad (2)$$

with V_n the volume of the nth particle (i.e., $\hat{x} = \hat{D}$ or $\hat{x} = \hat{H}$ is the x^3-weighted average diameter or height). This weighting allows one to take into account the size and shape distributions of the particles assembly. An in-plane diameter $\hat{D}$ equal to 8.2 nm was determined from the HAADF-STEM image by assuming a circular in-plane projected shape and the fitting parameter A in the dielectric function of Ag was set equal to 1. As seen in Fig. 6(b), a redshift of the SPR from $\lambda_\perp = 505$ nm ($\phi = 90°$) to $\lambda_\parallel = 550$ nm ($\phi = 0°$) is obtained with intermediate positions for different orientations ϕ of the electric field with respect to the particle lines. The model matches qualitatively the redshift of the band when decreasing ϕ from 90° to 0° (i.e., when decreasing the interparticle separation from 18.8 to 12.0 nm) (Refs. 40 and 41) because of near-field coupling (the far-field diffractive coupling effects are not taken into account since the periods $\langle L_\parallel \rangle$ and $\langle L_\perp \rangle$ are much smaller than the wavelength[42]). However, a discrepancy between the calculated spectral positions and the experimental ones remains with a shift amplitude between $\lambda_\perp$ and $\lambda_\parallel$ being twice smaller. Moreover, let us note a continuous shift in the simulations when ϕ decreases from 90° to 0° [Fig. 6(b)] while the experimental spectra exhibit a steady position down to 36° together with a modification of the width, of the asymmetry, and of the amplitude of the SPR [Fig. 6(a)]. This behavior is ascribed to the noncircular in-plane shape that can also produce an optical dichroism of the films.[7] Then the simulations have been performed assuming a set of ellipsoidal nanoparticles with weighted in-plane axis $\hat{D}_\parallel$ and $\hat{D}_\perp$, and weighted height $\hat{H}$ regularly distributed on a rectangular array of lattice parameters $\langle L_\parallel \rangle$ and $\langle L_\perp \rangle$ given in Table II. Only two directions of the electric field are presented in Fig. 7: parallel ($\phi = 0°$, dotted curve) and perpendicular to the lines of particles ($\phi = 90°$, solid curve). Accordingly, the amplitude of the splitting between the two SPR bands is more satisfactory when considering an assembly of aligned particles with an ellipsoidal shape, indicating that both the anisotropy of the spatial organization and the shape anisotropy of the particles are responsible for the optical dichroism.

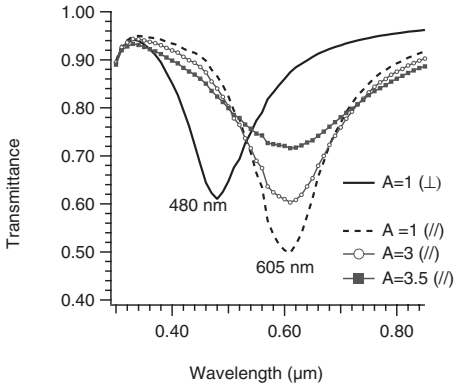

FIG. 7. Transmission calculations assuming a rectangular array of ellipsoidal Ag nanoparticles whose parameters ($\langle L_\parallel \rangle$, $\langle L_\perp \rangle$, $\hat{a}_\parallel$, $\hat{a}_\perp$, and $\hat{H}$) are given in Table II. Different weakening factors A are considered in the direction parallel ($A_\parallel$) to the ripples (see text).

A fairly good agreement in the amplitude, width, and position ($\lambda_\perp = 480$ nm) of the SPR band between experimental and calculated optical transmittance spectra is then obtained for the electric field perpendicular to the lines ($\phi = 90°$). For $\phi = 0°$, the calculated SPR band is slightly redshifted compared to the experimental one, nevertheless discrepancies are evidenced concerning the amplitude and width. Size and shape polydispersities can lead to a broadening and damping of the resonance. As can be seen from Table II, the ratios $\frac{\sigma_{D_\parallel}}{\langle D_\parallel \rangle}$ and $\frac{\sigma_{D_\perp}}{\langle D_\perp \rangle}$ are of the same order (0.28 and 0.29, respectively), indicating that this effect is not at the origin of the amplitude and width discrepancies between the SPR bands. Actually, the broadening and damping of the experimental transmission curve can be artificially reproduced in the model by varying the damping factor A in the dielectric function of silver,[7] which usually reflects the intensity of the size effects and depends on the nature of the particle/matrix interface. Therefore, in the simulations presented in Fig. 7, the dielectric function of Ag was modified by using a direction-dependent parameter A which was fixed to $A_\perp = 1$ for $\phi = 90°$ while $A_\parallel$ was adjusted up to 3.5 for $\phi = 0°$ in order to simulate the experimental broadening and damping of the SPR band, attesting a strong influence of the electromagnetic environment of the particles in this direction. It should be noted that the model used for the simulations does not take into account multipolar interactions between the particles. Now, the interaction intensity is linked to the amplitude of the electric field generated by the particles considered as point multipoles.[7] The amplitude f_m of the electric field generated by the multipole of order m ($m = 1$: dipole, $m = 2$: quadrupole,…) is known to vary as

$f_m=(D/2L)^{2m+1}$, L being the distance between the particles and D their diameter, i.e., their characteristic size. One obtains here $f_{1\|}=0.062$ and $f_{2\|}=0.0097$ for $\phi=0°$ (i.e., by using $D=\hat{D}_\|=9.5$ nm and $L=\langle L_\| \rangle=12$ nm), and $f_{1\perp}=0.0086$ and $f_{2\perp}=0.00036$ for $\phi=90°$ (i.e., by using $D=\hat{D}_\perp=7.7$ nm and $L=\langle L_\perp \rangle=18.8$ nm). It suggests that the interactions between nanoparticles result mainly from dipole-dipole contributions in the direction perpendicular to the lines ($f_{1\perp}/f_{2\perp}=23.9$) whereas the quadrupole contribution in the parallel direction is not negligible ($f_{1\|}/f_{2\|}=6.4$) and has the same magnitude as the dipole contribution in the perpendicular direction ($f_{2\|}\approx f_{1\perp}$). This is consistent with the edge-to-edge separation distances $s_\|=\langle L_\| \rangle-\hat{D}_\|$ between the particles within the lines equal to 2.5 nm, which corresponds to a $s_\|/\hat{D}_\|$ ratio of 0.26 whereas in the perpendicular direction $s_\perp=11.1$ nm and $s_\perp/\hat{D}_\perp=1.44$. This confirms that the electromagnetic environment of the particles along the particles lines differs from the one perpendicular to the lines. Therefore, the asymmetric shape of the resonance when the field is parallel to the ripples ($\phi=0°$) most probably originates from the proximity of the particles. In this direction, the optical behavior of the nanocomposite is similar to that of a 2D assembly of particles near the percolation threshold.[43] At last, the modifications of the width, of the asymmetry, and of the amplitude of the experimental SPR band when varying the orientation ϕ of the polarization of the light [Fig. 6(a)] can be explained as follows: due to the anisotropic shape of the particles, two SPR bands are expected as soon as the field is not parallel or perpendicular to the ripples. Nevertheless, due to the strong weakening of the SPR for a polarization parallel to the ripples, its contribution is weak for angles $\phi>36°$. Thus, the spectral position of the SPR tends to remain at the position $\lambda_\perp=485$ nm but with a decreasing amplitude and an increasing asymmetrical shape. For $\phi=18°$, the weight of the parallel contribution is no more negligible and a mix of the two SPR is visible.

3. *Optical properties: Simulations*

Our experimental results show that it is possible to control the electromagnetic environment of the nanoparticles by varying the etching conditions (ion energy, etching duration, and nature of the dielectric material) as shown in Table I but also suggest that the elaboration conditions of the nanocomposite film (shadowing angle, nature and quantity of metal) can also modify the shape and spatial organization of the nanoparticles. In Fig. 8 we present calculated data that evidence the effects of some parameters, which can be modified in order to control the spectral position of the SPR bands and the optical dichroism of the silver nanoparticle arrays. First of all, one would consider changing the dielectric host as we suggested in the first part of the paper: as already mentioned in the literature,[7] the increase in the refractive index of the dielectric host will produce a redshift of the SPR bands. This effect is illustrated in Fig. 8(a) where we have considered silver nanoparticles with a morphology and a spatial organization identical to those given in Table II. Nevertheless, we have shown in previous papers[10,11] that the shape of silver nanoparticles deposited on flat surfaces strongly depends on

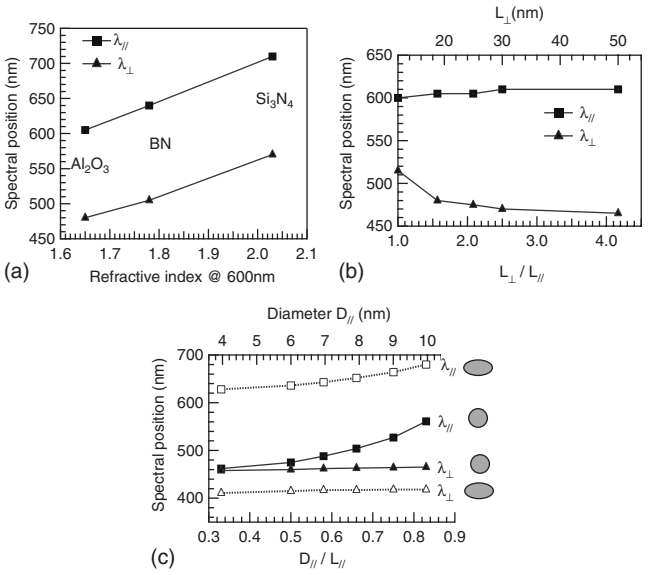

FIG. 8. (a) Calculated spectral position of the SPR bands (parallel and perpendicular to the ripples) as a function of the refractive index of the dielectric host (buffer and capping). The morphology and organization of the Ag particles are those given in Table II. (b) Calculated spectral position of the SPR bands (parallel and perpendicular to the ripples) as a function of the distance $L_\perp$ of the nanoparticles perpendicular to the ripples and with $L_\|=12$ nm. The morphology of the Ag particles are those given in Table II. (c) Calculated spectral position of the SPR bands (parallel and perpendicular to the ripples) as a function of the $\frac{D_\|}{L_\|}$ ratio of the nanoparticles: (full symbols) the Ag particles are assumed to be spherical (i.e., $D_\|=D_\perp=H$) and (open symbols) the Ag particles are assumed to be ellipsoidal (i.e., $D_\|=2D_\perp$ and $D_\perp=H$). The distances between particles $L_\|$ and $L_\perp$ are those given in Table II.

the dielectric capping layer. As a consequence, the calculated redshift obtained when changing the capping layer from BN to Al_2O_3 and then to Si_3N_4 would be influenced by the flattening of the particles. As we have shown in Sec. III A, it is possible to adjust the ripples period by changing the etching conditions. In Fig. 8(b), we present the variation in the spectral position of the SPR bands with the distance $L_\perp$ of the nanoparticles perpendicular to the ripples. The morphology of the Al_2O_3-capped particles is the one given in Table II and the interparticle distance parallel to the ripples is kept constant $L_\|=12$ nm (i.e., within the assumption that the same amount of silver will give the same particle morphology when the metal is deposited on a nanopatterned buffer layer with a different ripple period). In this case, as expected, starting from a square array of ellipsoidal silver nanoparticles, the spectral position of the SPR band $\lambda_\|$ remains the same while $\lambda_\perp$ is blueshifted owing to a decrease in the particle interactions in this direction. From previous studies,[10,11] when varying the amount of deposited silver, one should expect a modification of the size and shape of the nanoparticles (i.e., small nanoparticles on a flat surface are more spherical than larger ones) inducing a modification on the interparticle distance $L_\|$. In Fig. 8(c) we show the influence of the $\frac{D_\|}{L_\|}$ ratio on the optical dichroism for spherical (full symbols) and ellipsoidal (open symbols) particles, the distances between par-

ticles being those given in Table II: $L_{\parallel}=12$ nm and $L_{\perp}=18.8$ nm. While $\lambda_{\perp}$ remains quasiconstant, $\lambda_{\parallel}$ is strongly influenced by the $\frac{D_{\parallel}}{L_{\parallel}}$ ratio, the splitting between the SPR bands increasing with $\frac{D_{\parallel}}{L_{\parallel}}$ (i.e., when the particles size increases) and being emphasized when the particle shape is nonspherical as obtained in the experimental section.

IV. CONCLUSION

In conclusion, we have completed a study of Ag nanoparticles deposited at grazing angle on a rippled dielectric surface. We have shown first that nanopatterns on several dielectric amorphous thin films (Al_2O_3, BN, and Si_3N_4) can be obtained by Xe^+ ion etching at 55° with respect to the surface normal. The characteristics of the ripples (period, amplitude, and profile asymmetry) depend on the etching energy and duration and on the etched material, showing the large range of etching conditions that can be used to obtain nanopatterned surface on which arrays of metallic nanoparticles can be elaborated. Then, by shadowing effect of the ripples, we have demonstrated that the nucleation of silver atoms during the deposition takes place along the ripples leading to a self-organization of nanoparticles. We have experimentally evidenced that for a silver effective thickness of 2 nm, the so-obtained particles are ellipsoidal with a major axis parallel to the ripples. Both this anisotropy of shape and in-plane organization govern the anisotropic optical properties of the nanocomposite film. Then, experimental results and calculations have shown that is possible to control the amplitude of the splitting between the SPR bands (parallel and perpendicular to the ripples) by varying the nature of the dielectric material, the ion energy during the nanopatterning of the buffer layer (and therefore the distance perpendicular to the ripples), the quantity of metal (and therefore the size and shape of the particles and the distance between the particles inside a line).

ACKNOWLEDGMENTS

The authors are very grateful to J.-P. Simon for fruitful discussions and for his assistance during the GISAXS measurements. We also wish to acknowledge the technical support from all the D2AM staff.

APPENDIX

A model based on the Yamaguchi theory[38] is used to determine the dielectric function of the nanocomposite layer. We consider a set of identical nanoparticles distributed on a substrate. The effective dielectric function ϵ_{eff} of the nanocomposite layer connects the macroscopic polarization $\vec{P}$ and the macroscopic electric field $\overrightarrow{E_{ext}}$,

$$\vec{P} = \epsilon_0(\epsilon_{\text{eff}} - \epsilon_{\text{cap}})\overrightarrow{E_{ext}}, \tag{A1}$$

where ϵ_0 is the void permittivity and ϵ_{cap} is the dielectric function of the capping film.

In other respects, the macroscopic polarization $\vec{P}$ is the sum of the microscopic polarizations $\vec{p}$ of the particles: $\vec{P}=N\vec{p}$, where N is the number of particles per volume unit. $\vec{P}$ can be expressed as

$$\vec{P} = N\epsilon_0\epsilon_{\text{cap}}V\alpha\overrightarrow{E_{loc}}, \tag{A2}$$

where αV is the polarizability of the particle of volume V and with $\alpha=\frac{\epsilon_m-\epsilon_{\text{cap}}}{\epsilon_{\text{cap}}+\ell(\epsilon_m-\epsilon_{\text{cap}})}$ (where ℓ is the geometrical depolarization factor[7] of the ellipsoidal nanoparticle and ϵ_m is the dielectric function of the metal) and $\overrightarrow{E_{loc}}$ is the local field seen by one central particle. This field results in three contributions: the macroscopic applied electric field $\overrightarrow{E_{ext}}$, the field created by the image dipole $\overrightarrow{E_{im}}$ of the particle, and the field created by neighboring particles and their images $\overrightarrow{E_{int}}$.

Let us recall that the field $\overrightarrow{E_{dip}}$ created by a dipole $\vec{p}$ set in O at a distance r from a point M in a medium of dielectric function ϵ_{ext} is given by

$$\overrightarrow{E_{dip}} = \frac{1}{4\pi\epsilon_0\epsilon_{ext}} \times \frac{3(\vec{p}\,.\,\vec{u_r})\vec{u_r} - \vec{p}}{r^3}, \tag{A3}$$

where $\vec{u_r}$ is a unit vector defined as $\overrightarrow{OM}=r\vec{u_r}$.

Therefore, the different contributions to the local field $\overrightarrow{E_{loc}}$ seen by a central particle can be obtained, when considering dipolar interactions, with: the field created by the dipole image given by

$$\overrightarrow{E_{im}} = \frac{1}{4\pi\epsilon_0\epsilon_{\text{cap}}H^3} \times \frac{\epsilon_{sub}-\epsilon_{\text{cap}}}{\epsilon_{sub}+\epsilon_{\text{cap}}}\vec{p}, \tag{A4}$$

This field is nil if the substrate is identical to the capping material, i.e., $\epsilon_{sub}=\epsilon_{\text{cap}}$. The contribution $\overrightarrow{E_{int}}=\vec{E}_{neighb}+\vec{E}_{im\ neighb}$ of the neighboring particles ($\vec{E}_{neighb}$) and their images ($\vec{E}_{im\ neighb}$) is given by

$$\vec{E}_{neighb} = \frac{1}{4\pi\epsilon_0\epsilon_{\text{cap}}}\sum_j \frac{3(\vec{p_j}\,.\,\vec{u_{r_j}})\vec{u_{r_j}} - \vec{p_j}}{r_j^3} \tag{A5}$$

and

$$\vec{E}_{im\ neighb} = \frac{1}{4\pi\epsilon_0\epsilon_{\text{cap}}}\sum_j \frac{3(\vec{p_j'}\,.\,\vec{u_{r_j}'})\vec{u_{r_j}'} - \vec{p_j'}}{r_j'^3}, \tag{A6}$$

where $\vec{p_j'}$ is the dipolar moment of the image dipoles of the neighboring particles. These dipoles are located at a distance r_j' from the central particle.

With the assumption that all the nanoparticles have the same dipolar moment $\vec{p}=\vec{p_j}$ (i.e., the same polarizability), the local field can be written as

$$\overrightarrow{E_{loc}} = \frac{\overrightarrow{E_{ext}}}{1+\epsilon_0\epsilon_{\text{cap}}\alpha\beta}, \tag{A7}$$

where

$$\beta = \frac{V}{4\pi\epsilon_0\epsilon_{\text{cap}}} \times \left[\frac{-1}{H^3} \times \frac{\epsilon_{sub} - \epsilon_{\text{cap}}}{\epsilon_{sub} + \epsilon_{\text{cap}}} - \sum_j \frac{3\cos^2\theta_j - 1}{r_j^3} - \frac{\epsilon_{sub} - \epsilon_{\text{cap}}}{\epsilon_{sub} + \epsilon_{\text{cap}}} \times \sum_j \frac{3\cos^2\theta_j' - 1}{r_j'^3} \right] \tag{A8}$$

and θ_j (respectively, θ_j') is the angle between $\vec{u_j}$ (respectively, $\vec{u_j'}$) and $\vec{p_j}$ (respectively, $\vec{p_j'}$).

The terms $C=\sum_j \frac{3\cos^2\theta_j - 1}{r_j^3}$ and $C' = \sum_j \frac{3\cos^2\theta_j' - 1}{r_j'^3}$ account for the contribution to the local field of the neighboring nanoparticles and their images. For nanoparticles regularly located on a rectangular array, C and C' depend on the particles height H and lattice parameters $\langle L_\parallel \rangle$ and $\langle L_\perp \rangle$.

Therefore the dielectric function of the effective medium can be obtained from Eqs. (A1) and (A2)

$$\epsilon_0(\epsilon_{\text{eff}} - \epsilon_{\text{cap}})\overrightarrow{E_{ext}} = N\epsilon_0\epsilon_{\text{cap}} V \alpha \overrightarrow{E_{loc}} = N\epsilon_0\epsilon_{\text{cap}} V \frac{\epsilon_{\text{m}} - \epsilon_{\text{cap}}}{\epsilon_{\text{cap}} + \ell(\epsilon_{\text{m}} - \epsilon_{\text{cap}})} \overrightarrow{E_{loc}}. \tag{A9}$$

Using Eq. (A7), one obtains

$$\epsilon_0(\epsilon_{\text{eff}} - \epsilon_{\text{cap}}) = NV \frac{\epsilon_{\text{cap}}(\epsilon_{\text{eff}} - \epsilon_{\text{cap}})}{\epsilon_{\text{cap}} + \ell(\epsilon_{\text{m}} - \epsilon_{\text{cap}})} \times \frac{1}{1 + \epsilon_0\epsilon_{\text{cap}}\alpha\beta}. \tag{A10}$$

The effective dielectric function of the nanocomposite layer is then given by

$$\epsilon_{\text{eff}} = \epsilon_{\text{cap}} \left[q \frac{\epsilon_{\text{m}} - \epsilon_{\text{cap}}}{\epsilon_{\text{cap}} + F(\epsilon_{\text{m}} - \epsilon_{\text{cap}})} + 1 \right], \tag{A11}$$

where $q=NV$ and $F = \frac{\epsilon_0\epsilon_{\text{cap}}^2}{\epsilon_{\text{m}} - \epsilon_{\text{cap}}}\alpha\beta + \ell(1 + \epsilon_0\epsilon_{\text{cap}}\alpha\beta)$ is the effective depolarization factor, which takes into account the shape of particles, the interparticle dipolar interactions, and the interactions with the substrate.

*sophie.camelio@univ-poitiers.fr
†Present address: Laboratoire de Chimie de la Matière Condensée de Paris, Université P. et M. Curie–Paris 6/CNRS–UMR 7574/ENSCP, France.

[1] V. M. Shalaev and S. Kawata, *Nanophotonics With Surface Plasmons* (Springer, Berlin, 2007).
[2] P. G. Kik and M. L. Brongersma, *Surface Plasmon Nanophotonics* (Springer, Berlin, 2007).
[3] S. A. Maier, *Plasmonics: Fundamentals and Applications* (Springer, New York, 2007).
[4] K. A. Willets and R. P. Van Duyne, Annu. Rev. Phys. Chem. **58**, 267 (2007).
[5] A. J. Haes and R. P. Van Duyne, J. Am. Chem. Soc. **124**, 10596 (2002).
[6] N. Félidj, J. Aubard, G. Lévi, J. R. Krenn, M. Salerno, G. Schider, B. Lamprecht, A. Leitner, and F. R. Aussenegg, Phys. Rev. B **65**, 075419 (2002).
[7] U. Kreibig and M. Vollmer, in *Optical Properties of Metal Particles*, edited by U. Kreibig and M. Vollmer (Springer, Berlin, 1995).
[8] C. F. Bohren and D. R. Huffman, in *Absorption and Scattering of Light by Small Particles*, edited by C. F. Bohren and D. R. Huffman (Wiley, New York, 1983).
[9] S. Camelio, J. Toudert, D. Babonneau, and T. Girardeau, Appl. Phys. B: Lasers Opt. **80**, 89 (2005).
[10] J. Toudert, S. Camelio, D. Babonneau, M.-F. Denanot, T. Girardeau, J. P. Espinos, F. Yubero, and A. R. Gonzalez-Elipe, J. Appl. Phys. **98**, 114316 (2005).
[11] D. Lantiat, D. Babonneau, S. Camelio, F. Pailloux, and M.-F. Denanot, J. Appl. Phys. **102**, 113518 (2007).
[12] D. Babonneau, D. Lantiat, S. Camelio, L. Simonot, F. Pailloux, M.-F. Denanot, and T. Girardeau, Eur. Phys. J.: Appl. Phys. **44**, 3 (2008).
[13] A. Sugawara and M. R. Scheinfein, Phys. Rev. B **56**, R8499 (1997).
[14] V. Repain, G. Baudot, H. Ellmer, and S. Rousset, Mater. Sci. Eng., B **96**, 178 (2002).
[15] O. Fruchart, G. Renaud, A. Barbier, M. Noblet, O. Ulrich, J.-P. Deville, F. Scheurer, J. Mane-Mane, V. Repain, G. Baudot, and S. Rousset, Europhys. Lett. **63**, 275 (2003).
[16] Y. F. Guan and A. J. Pedraza, Nanotechnology **16**, 1612 (2005).
[17] E. Fort, C. Ricolleau, and J. Sau-Pueyo, Nano Lett. **3**, 65 (2003).
[18] T. W. H. Oates, A. Keller, S. Facsko, and A. Mücklich, Plasmonics **2**, 47 (2007).
[19] T. W. H. Oates, A. Keller, S. Noda, and S. Facsko, Appl. Phys. Lett. **93**, 063106 (2008).
[20] F. Cuccureddu, S. Murphy, I. V. Shvets, M. Porcu, and H. W. Zandbergen, Nano Lett. **8**, 3248 (2008).
[21] S. Camelio, D. Babonneau, D. Lantiat, and L. Simonot, EPL **79**, 47002 (2007).
[22] A. Toma, D. Chiappe, D. Massabò, C. Boragno, and F. Buatier de Mongeot, Appl. Phys. Lett. **93**, 163104 (2008).
[23] T. M. Mayer, E. Chason, and A. J. Howard, J. Appl. Phys. **76**, 1633 (1994).
[24] C. C. Umbach, R. L. Headrick, and K.-C. Chang, Phys. Rev. Lett. **87**, 246104 (2001).
[25] G. Carter and V. Vishnyakov, Phys. Rev. B **54**, 17647 (1996).
[26] E. Chason, T. M. Mayer, B. K. Kellerman, D. T. McIlroy, and A. J. Howard, Phys. Rev. Lett. **72**, 3040 (1994).
[27] B. Ziberi, F. Frost, Th. Höche, and B. Rauschenbach, Phys. Rev. B **72**, 235310 (2005).
[28] S. Rusponi, C. Boragno, and U. Valbusa, Phys. Rev. Lett. **78**, 2795 (1997).
[29] U. Valbusa, C. Boragno, and F. Buatier de Mongeot, J. Phys.:

Condens. Matter **14**, 8153 (2002).
[30] W. L. Chan and E. Chason, J. Appl. Phys. **101**, 121301 (2007).
[31] H. Zhou, Y. Wang, L. Zhou, R. L. Headrick, A. S. Özcan, Y. Wang, G. Özaydin, K. F. Ludwig, Jr., and D. P. Siddins, Phys. Rev. B **75**, 155416 (2007).
[32] M. Rauscher, R. Paniago, H. Metzger, Z. Kovats, J. Domke, J. Peisl, H.-D. Pfannes, J. Schulze, and I. Eisele, J. Appl. Phys. **86**, 6763 (1999).
[33] Homemade routine developed by D. Babonneau (unpublished).
[34] F. Leroy, R. Lazzari, and G. Renaud, Acta Crystallogr., Sect. A: Found. Crystallogr. **60**, 565 (2004).
[35] S. A. Bradley, M. J. Cohn, and S. Pennycook, Microsc. Res. Tech. **28**, 427 (1994).
[36] V. Holý and T. Baumbach, Phys. Rev. B **49**, 10668 (1994).
[37] M. M. A. Kashem, J. Perlich, L. Schulz, S. V. Roth, and P. Muller-Buschbaum, Macromolecules **41**, 2186 (2008).
[38] T. Yamaguchi, S. Yoshida, and A. Kinbara, Thin Solid Films **21**, 173 (1974).
[39] H. Hövel, S. Fritz, A. Hilger, U. Kreibig, and M. Vollmer, Phys. Rev. B **48**, 18178 (1993).
[40] K.-H. Su, Q.-H. Wei, X. Zhang, J. J. Mock, D. R. Smith, and S. Schultz, Nano Lett. **3**, 1087 (2003).
[41] P. K. Jain and M. A. El-Sayed, J. Phys. Chem. C **112**, 4954 (2008).
[42] N. Félidj, G. Laurent, J. Aubard, G. Lévi, A. Hohenau, J. R. Krenn, and F. R. Aussenegg, J. Chem. Phys. **123**, 221103 (2005).
[43] Q.-Q. Wang, J.-B. Hun, S. Ding, G.-G. Xiong, and D.-C. Tian, Appl. Surf. Sci. **243**, 329 (2005).